

# Locking Oxygen in Lattice: A Quantifiable Comparison of Gas Generation in Polycrystalline and Single Crystal Ni-Rich Cathodes

Jiangtao Hu,<sup>1,‡</sup> Linze Li,<sup>2</sup> Yujing Bi,<sup>1</sup> Jinhui Tao,<sup>3</sup> Joshua Lochala,<sup>1</sup> Dianying Liu,<sup>1</sup> Bingbin Wu,<sup>1</sup> Xia Cao,<sup>1</sup> Sujong Chae,<sup>1</sup> Chongmin Wang,<sup>2</sup> Jie Xiao<sup>\*1,4</sup>

<sup>1</sup> Energy and Environment Directorate, Pacific Northwest National Laboratory, Richland, WA 99354, USA. <sup>‡</sup>*Current address:* College of Chemistry and Environmental Engineering, Graphene Composite Research Center, Shenzhen University, Shenzhen, 518060, PR China

<sup>2</sup> Environmental Molecular Sciences Laboratory, Pacific Northwest National Laboratory, Richland, WA 99354, USA

<sup>3</sup> Physical and Computational Sciences Directorate, Pacific Northwest National Laboratory, Richland, WA 99354, USA

<sup>4</sup> Department of Materials Science & Engineering, University of Washington, Seattle, WA 98195, USA

\*e-mail: [jie.xiao@pnnl.gov](mailto:jie.xiao@pnnl.gov)

*Keywords:* Ni-rich NMC, Oxygen release, Gas generation, Quantification analysis

**Abstract:** High-energy Ni-rich NMC ( $\text{LiNi}_x\text{Mn}_y\text{Co}_{1-x-y}\text{O}_2$ ,  $x \geq 0.6$ ) is a very promising cathode material in Li-ion batteries but the gas generation during cycling is a significant safety concern and becomes the major roadblock of the large-scale commercialization of Ni-rich NMC cathode materials. Micron-sized single crystal Ni-rich NMC has a potential to address the common issues that polycrystals have. However, it is unknown if gassing issue will be mitigated or even eliminated by using single crystals, not mentioning a quantifiable understanding of gas generation from single crystals and polycrystals. This work takes  $\text{LiNi}_{0.76}\text{Mn}_{0.14}\text{Co}_{0.1}\text{O}_2$  (NMC76) as a model material to study the mechanism of gas generation from single crystal and polycrystalline NMC by using both coin cells and pouch cells, which provides different conclusions on the generated gases, highlighting the importance of using relevant testing conditions for fundamental diagnostic study on battery materials. The information from single crystal NMC also provides critical insights from material perspective to enhance the safety attributes of Ni-rich NMC cathodes.

## Introduction

Ni-rich cathode, e.g.,  $\text{LiNi}_x\text{Mn}_y\text{Co}_{1-x-y}\text{O}_2$  (NMC,  $x \geq 0.6$ ) materials, have been investigated intensively as one of the most promising cathode materials for next-generation high energy Li-ion batteries (LIBs) for vehicle electrification. However, challenges exist for large-scale deployment. As more Ni is incorporated in the lattice, the material surfaces become more active, increasing both electrochemical and chemical reactivities of Ni-rich NMC in contact with electrolyte.<sup>[1, 2]</sup> NMC usually adopts a conventional morphology of secondary structure meaning numerous nano-sized primary particles aggregate together to form a larger particle. These agglomerated NMC particles have their unique advantages of shortening  $\text{Li}^+$  diffusion pathway<sup>[3]</sup> as well as improved power<sup>[4]</sup>. Particle cracking along the grain boundaries among primary particles is also found after cycling due to the anisotropic volume expansion among different primary particles.<sup>[5-10]</sup> In Ni-rich NMC, the particle pulverization continuously exposes new surfaces to the electrolyte during cycling, accelerating side reactions already worsened by increased Ni within the lattice. Alternatively, single crystal Ni-rich NMC has been proposed to overcome the particle cracking problem and is expected to be more tolerant towards moisture attack with improved safety attributes.<sup>[11, 12]</sup> Although microcracking evolved from lattice gliding is also seen,<sup>[13]</sup> it is believed that the gliding and microcracking is much less significant than in agglomerated secondary particles and can be stabilized within particles. While quite a few good publications are elaborating on the origin of gases detected in Ni-rich NMC, the scientific questions that remain unclear. Here, we will focus on the four following questions by comparing single crystal and polycrystalline  $\text{LiNi}_{0.76}\text{Mn}_{0.14}\text{Co}_{0.10}\text{O}_2$  (NMC76) in functioning electrochemical cells: (1) What drives gases generation? (2) Are the gases continuously produced or only in the beginning? (3) The fundamental relationship between detected gas and the number of grain boundaries in Ni-rich NMC? (4) Can we quantify the amounts of different gases that evolved at different cycles to understand surface reactions better?

## Results and Discussion

We firstly develop a standard procedure of using *in situ* Differential Electrochemical Mass Spectrometry (DEMS) to ensure all results are repeatable for evaluating and quantifying different gases in Ni-rich NMC (**Fig. 1a**). While DEMS is broadly used for gas detection, there are a few steps worthy of attention in order to get consistent results for online gas monitoring. For example, the capillary that allows gas to diffuse from the electrochemical cell (E-cell) to MS is usually

narrow but long (2 m in length and 0.05 mm in diameter in this case). Therefore, a time delay will occur between gas generated in the cell and detected by DEMS. By using the controlled flow rate (12.5  $\mu\text{L}/\text{min}$ ), the time gap (18.84 s) can be calculated and used to identify the real onset potential when each gas is generated (Fig. 1a). All gases have certain solubilities in the electrolyte, especially for  $\text{CO}_2$ ; its solubility is as high as ca.  $8.7 \times 10^{-3}$  mole fraction in organic electrolyte,<sup>[14]</sup> which further affects the time resolution and quantification of  $\text{CO}_2$  detected by DEMS. The detailed testing procedures and parameters that improve the repeatability of gas measurement have been provided in **Table S1** and **Experimental section**.

Using the procedure developed in this work, the onset potentials of gases generated from different Ni-rich NMC crystals (polycrystalline and single crystal) are firstly compared. The electrolyte used in this work is 1M  $\text{LiPF}_6$  in EC/EMC (3:7 in weight). Without Ni-rich NMC cathode, this carbonate electrolyte itself is quite stable below 4.9 V (Fig. S1). Only above 4.9 V, gases are detected in this carbonate electrolyte which directly contacts with current collector, consistent with previously reported results.<sup>[15, 16]</sup> The stability of this electrolyte suggests that the majority of gases captured in a cell before 4.9 V are triggered by the electrode/electrolyte interfacial reaction instead of by the decomposition of the frequently applied carbonate electrolyte. The two different Ni-rich NMC76 crystals in contact with the same electrolyte are firstly charged to 4.3 V. From 4.3 to 4.8 V, the potentials applied on the E-cell are gradually elevated with a step size of 0.1 V (**Fig. 1b,c**). Four different gases, i.e.,  $\text{CO}_2$ , CO,  $\text{O}_2$ , and  $\text{H}_2$ , have been detected in both cases during charge. For polycrystalline NMC76, the onset voltages of  $\text{CO}_2$ , CO,  $\text{O}_2$ , and  $\text{H}_2$  evolution are 3.95 V, 4.4 V, 4.5 V and 4.7 V, respectively (Fig. 1b). Compared to polycrystalline NMC76, single crystal NMC76 displays higher onset voltages for each gas. For example,  $\text{O}_2$  does not show up until 4.7 V (Fig. 1c) in single crystals, while it is detected at 4.5 V from polycrystals.

$\text{CO}_2$  is always the first gas detected in both cases, and the early onsets (before 4.0 V, **Fig. S2**) are assigned to the residual surface carbonate salts that arise from material synthesis and/or during storage.<sup>[17, 18]</sup> A substantial increase of  $\text{CO}_2$  content is found, because oxygen release is easy to occur from cathode lattice at high charge state, leading to an intensified interface reaction with electrolyte.<sup>[16, 19, 20]</sup> For polycrystalline NMC76,  $\text{CO}_2$  induced by the side reaction occurs as early as ca. 4.25 V (vs.  $\text{Li}/\text{Li}^+$ ) much lower than single crystal NMC76 (after 4.4 V). The overall impact of the interfacial regions between electrolyte and electrode material increases with decreasing

primary particle size. The nano-sized primary particles in polycrystalline NMC76 provide more reactive sites to interact with electrolytes during cycling than micron-sized single crystal NMC76 (see *in situ* AFM in **Video S1,2**). Even for single crystal, there is a sharp increase of CO<sub>2</sub> generation rate beyond 4.4 V. In both cases, a trace amount of CO is also detected, accompanied by the generation of CO<sub>2</sub>, and aligns well with the trend of CO<sub>2</sub> evolution (Fig. 1b,c). The almost simultaneous evolution of CO<sub>2</sub>/CO is a good indicator of O release from the lattice, which chemically reacts with the electrolyte producing CO<sub>2</sub> and CO concurrently.<sup>[16, 19]</sup> O<sub>2</sub> is also found to evolve at 4.5 V and 4.7 V for polycrystalline and single crystal NMC76, respectively, indicating that part of O escaped from NMC76 lattice recombines to produce O<sub>2</sub> gas.<sup>[19, 21]</sup> The signal of H<sub>2</sub> is ignorable in the background noise until 4.7 V (for polycrystalline NMC76) or 4.8 V (for single crystal NMC76). At such high voltages, a solvent such as ethylene carbonate (EC) is vigorously oxidized to produce protic species R-H<sup>+</sup>, which are reduced on the anode side, strongly enhancing H<sub>2</sub> evolution.<sup>[22]</sup> While R-H<sup>+</sup> occurs at a similar time with CO<sub>2</sub>, because they are both from the side reactions between NMC and electrolyte.<sup>[22, 23]</sup> The onset potential of H<sub>2</sub> is delayed by a few hours compared to the generation of R-H<sup>+</sup> (**Table S2**), which depends on both the integrity of the anode SEI and the actual concentration of protons.<sup>[22]</sup> As concluded in **Fig. 1f**, a higher electrochemical driving force is generally needed for single crystal NMC76 to release gas, compared to its polycrystalline counterpart.

The morphological changes of polycrystalline and single crystal NMC76 after the first charge are probed by using *in situ* AFM (**Video S1,2**). As potential increases to 4.5 V, **new boundaries are immediately found among primary particles of polycrystal NMC76 (arrow in Fig. 1d)**, while single crystal NMC76 shows almost no change (**Fig. 1e**). At a high voltage of 4.9 V, gliding within an individual single crystal is seen.<sup>[13]</sup> Considering the fact that most practical cells will not go beyond 4.5 V in full cells, single crystal NMC76, compared to polycrystalline, will undergo a minimum increase of new boundaries or surface areas within regular electrochemical window, consistent with the observed gas evolution in Fig. 1b,c.

**While valuable information has been reported in understanding the gas generated in NMC materials, a key piece missing is whether, gases especially O<sub>2</sub> and H<sub>2</sub> are only generated in the first few cycles or continuously produced over extensive cycling. This knowledge will provide important clues in understanding and enhancing materials' safety attributes.** Polycrystalline and

single crystal NMC76 studied in this work have average particle sizes of ca. 7  $\mu\text{m}$  and 3  $\mu\text{m}$ , respectively (**Fig. 2a,c**).  $\text{CO}_2$ ,  $\text{H}_2$ , and  $\text{O}_2$  gases detected at different cycles of polycrystalline and single crystal NMC76 are compared in **Fig. 2b,d**. For polycrystalline NMC76, the detected amount of  $\text{CO}_2$  is highest in the first cycle, mainly derived from the decomposition of residual lithium carbonate salt on the NMC surface. During the 2<sup>nd</sup> and 3<sup>rd</sup> cycle, the corresponding onset potentials of  $\text{CO}_2$  generation are 4.28 V and 4.29 V, respectively, which is from chemical reactions between active lattice oxygen and electrolyte.<sup>[16, 19, 20]</sup>  $\text{H}_2$  evolution can be assigned to the reduction of oxidized aprotic solvent (originally generated on the cathode side) on the anode. As discussed earlier, there is a time delay for  $\text{H}_2$  detection. The cells for DEMS in Fig. 2b,d are cycled between 2.7 and 4.5 V, and  $\text{R-H}^+$  will be generated during the charge process, which is reduced on the anode side to produce  $\text{H}_2$  and to be detected later. The time gap between  $\text{R-H}^+$  production and  $\text{H}_2$  detection (**Table S2**) corresponds to the  $\text{H}_2$  detection potentials around the end of the discharge (3<sup>rd</sup> panels in Fig. 2b,d). Of note,  $\text{H}_2$  detected in this work should not come from the reduction of moisture in the cell because of the absence of  $\text{H}_2$  signal in the earlier initial electrochemical process.<sup>[24]</sup> In addition, the periodic occurrence of  $\text{H}_2$  gas throughout the entire 200 cycles also suggests that  $\text{H}_2$  is related to the electrolyte reaction driven by potentials. Compared to polycrystalline NMC76, the contents of  $\text{CO}_2$  and  $\text{H}_2$  produced from single crystal NMC76 are much less (**Fig. S3a,b**). After 50 and even 200 cycles (**Fig. S4**),  $\text{CO}_2$  and  $\text{H}_2$  gases are still captured from both polycrystalline and single crystal NMC76, although the amounts of gases detected from cycled single crystal are largely reduced compared to those from polycrystals (Fig. S3a,b). A trace amount of  $\text{O}_2$  has been detected at 4.5 V during the first charge of polycrystalline NMC76, while there is no  $\text{O}_2$  from single crystal charging throughout the entire 200 cycles. After the formation cycle, the vanishing  $\text{O}_2$  signal in polycrystalline NMC76 is because of the fast chemical reaction between highly reactive O with carbonate solvent such as EC, which has been well documented in Li- $\text{O}_2$  battery study.<sup>[25-27]</sup> **To capture  $\text{O}_2$  signal in a working electrochemical cell, a more significant amount of O released in a short time is pre-requisite.<sup>[19]</sup> Mitigation of interfacial side reactions and eliminate lattice oxygen release especially to avoid the coexistence of  $\text{H}_2$  and  $\text{O}_2$  in the same cell is critical for enhancing battery safety from cathode aspect.**

Lowering the cutoff voltage of Graphite||NMC76 full cells to 4.2 V leads to stable cycling of both polycrystalline and single crystal NMC76. Both of them have greater than 80% of capacity retention after 500 cycles in full cells (**Fig. 3a**). Note that single crystal has much bigger sizes than

that of primary particles in polycrystalline NMC76. Therefore, the usable capacity of the former is slightly lower than that of the latter at a C/3 rate. Only CO<sub>2</sub> and H<sub>2</sub> are detected in both cases after extensive cycling (**Fig. S5**). The average CO<sub>2</sub> contents generated from polycrystalline and single crystal NMC76 after 200 cycles are 0.165 μmol g<sup>-1</sup> and 0.043 μmol g<sup>-1</sup>, respectively. If these full cells were charged up to 4.5 V, CO<sub>2</sub> detected from the polycrystals is high at 0.215 μmol g<sup>-1</sup>. (**Fig. S6**) Interestingly, CO<sub>2</sub> generated from single crystal is still low at 0.045 μmol g<sup>-1</sup>, showing a minimum increase even at 4.5 V. Similarly, after 200 cycles, around 0.108 μmol g<sup>-1</sup> and 0.045 μmol g<sup>-1</sup> of H<sub>2</sub> were produced, respectively, in polycrystalline and single crystal NMC76 (between 2.7 and 4.25 V). This gas production is lower than when tested in 4.5 V (0.124 μmol g<sup>-1</sup> for polycrystalline NMC76 and 0.05 μmol g<sup>-1</sup> for single crystal NMC76). To intensify the truth that polycrystalline NMC76 generates more gas than single crystal NMC76, we also normalized gas evolution by discharge capacity, which still obeys our conclusion, such as in the second cycle (**Fig. 2b and d**), that the gas evolution content per capacity from polycrystalline NMC76 is around 1.057 nmol/mAh, higher than that in single crystal (0.408 nmol/mAh).

A group of Graphite||NMC76 pouch cells were cycled between 2.65 and 4.45 V (vs. graphite) for 200 cycles, to help induce gas generation. The gradually generated gases are accumulated in a designed “gas room” in all the pouch cells. (**Fig. 3b**) Gas is expelled to MS with carrier gas from each pouch cell after cycling. Unlike in half coin cells, O<sub>2</sub> is now also detected from the pouch cells after 200 cycles (**Fig. 3c**). The prominent observation of O<sub>2</sub> in pouch cells compared to the Li-metal coin cells can be assigned to the absence of highly active Li metal, which reacts with O species in the cell. The significantly reduced electrolyte (3.19 μL g<sup>-1</sup> in pouch cell vs. 26.45 μL g<sup>-1</sup> in DEMS cell) in the pouch cell also mitigates the fast reactions between EC and O, making it possible to capture the accumulated O<sub>2</sub> during extensive cycling. The simultaneous occurrence of O<sub>2</sub> and H<sub>2</sub> in Li-ion batteries with polycrystalline NMC76 cathode may partially explain the reported safety issue, especially during thermal runaway.<sup>[28]</sup> A single-layer pouch cell consisting of graphite and single crystal NMC76 is also studied. Again, there is no O<sub>2</sub> found after 200 cycles which can be attributed to the limited surface area of single crystal NMC76 (onset potential for O<sub>2</sub> release: 4.7 V vs. Li<sup>+</sup>/Li in single crystals as shown in **Fig. 1c**). Therefore, single crystal Ni-rich cathode will greatly enhance the safety of Ni-rich NMC cathode because of the absence of the O<sub>2</sub>/H<sub>2</sub> couple below 4.45 V in full cell.

A closer inspection on the cycled polycrystalline NMC76 found that originally aggregated primary particles become loosely attached with many visible pores (yellow arrows in **Fig. 4a**). The internal structure further reveals an increased number of grain boundaries, compared with pristine polycrystals, due to the detachment among primary particles (**Fig. 4b**). Significant cracking is also seen, and the new surfaces are quickly exposed to the electrolyte through the cracks (inset of **Fig. 4b**), inducing more gas generation. After 200 cycles, the rock-salt structure formed on polycrystalline NMC76 is about 3-4 nm thick (**Fig. 4c** and **S7**), triggered by the loss of oxygen.<sup>[29-32]</sup> Electron energy loss spectroscopy (EELS) spectra of the O K-edges and Mn, Co, and Ni L-edges are collected at 5 different locations from particle surface to bulk. The almost disappeared pre-edge of O K-edge at the particle surface confirms the loss of oxygen,<sup>[33]</sup> which gradually increases and levels off when probed to a depth of 16 nm in cycled polycrystalline NMC76 (**Fig. 4g**), indicating O released from lattice initiates from the surface. As to the Mn, Co, and Ni L-edges, a clear shift to lower energy losses from bulk to surface is observed, corresponding to the decrease of the average valence state of TM cations to compensate for oxygen loss from the lattice.

In contrast, cycled single crystal NMC76 largely maintains a solid structure with some visible gliding marks (yellow arrows in **Fig. 4d**). The internal structure of the single crystal is still mostly integrated after 200 cycles (**Fig. 4e**), largely minimizing the possibility of exposing new surfaces to the electrolyte. However, a thin layer of rock-salt structure is indeed discovered from extensively cycled single crystal (**Fig. 4f** and **S8**) with a similar thickness of 3-4 nm as that formed on polycrystalline surfaces, confirmed by EELS spectra (**Fig. 4h**). Therefore, we did not attribute this rock-salt layer as the main reason for the reduced gas generation from single crystal NMC76, which can be attributed the physical difference between the two materials, including morphology and the crystallinity. The homogeneous element distribution in polycrystalline and single crystal NMC76 is well maintained after 200 cycles. The observed black vacancy clusters in polycrystalline NMC76 are introduced during the materials synthesis, rather than the electrochemical cycling (**Fig. S9**).<sup>[34]</sup>

The above direct observations on the formation of grain boundaries and oxygen vacancies due to O loss during cycling in polycrystalline NMC76 are consistent with the continuous CO<sub>2</sub> generation from polycrystals during cycling which mostly happens on the cathode side. In contrast,

H<sub>2</sub> generation involves both cathode and anode. Electrolyte screening and material design will help further reduce gas generation.<sup>[35, 36]</sup>

## Conclusions

A quantifiable comparison has been conducted to understand the origin and evolution of different gases, i.e., CO<sub>2</sub>, CO, O<sub>2</sub>, and H<sub>2</sub>, generated in polycrystalline and single crystal Ni-rich NMC. A higher electrochemical driving force is generally necessary for gas generation from single crystal compared to polycrystals. Even at elevated potentials, the amount of gases detected from single crystal is still much lower than polycrystals. Compared to polycrystals, the drastically reduced number of boundaries and surface area in single crystal suppresses surface side reactions, which mitigate gas generation. It is also found that O and thus O<sub>2</sub> is being accumulated in polycrystalline NMC76, which is only observable in full pouch cells tested at relevant conditions. The concurrence and accumulation of O<sub>2</sub> and H<sub>2</sub> after extensive cycling fundamentally explains the safety issue of Li-ion batteries utilizing polycrystalline NMC76 as the cathode, while single crystal material indicates a great pathway to enhance battery safety from a material perspective.

## Experimental Section

### Preparation of polycrystalline and single crystal LiNi<sub>0.76</sub>Mn<sub>0.14</sub>Co<sub>0.10</sub>O<sub>2</sub>

The synthesis of LiNi<sub>0.76</sub>Mn<sub>0.14</sub>Co<sub>0.10</sub>O<sub>2</sub> (NMC76), including secondary polycrystalline NMC76 and single crystal NMC76, can be referred to our previous works<sup>[5, 13]</sup>, and the corresponding BET surface area values are presented in **Fig. S10**.

### Electrochemical measurements

*Full coin cell.* The positive electrodes were prepared by mixing active materials (polycrystalline and single crystal NMC76), Super P (MTI Corporation) and polyvinylidene difluoride (PVDF, HSV1800 Supplied by Arkema Technical Polymers) with a weight ratio of 96:2:2 in N-methylpyrrolidone (NMP, Sigma-Aldrich), then they were coated on carbon coated Al foil. After dried at 80 °C overnight, the prepared electrodes were punched into round disks with a diameter of 1.27 cm. Before assembly, the punched electrodes were dried overnight at 120 °C under vacuum. Graphite anode was prepared by mixing graphite (BTR new energy materials INC.), sodium

carboxymethyl cellulose (CMC, MTI Corporation), styrene butadiene rubber (SBR, MTI Corporation) and Super P (MTI Corporation) with the weight ratio of 100:1.5:2.5:1, and then coated on Cu foil. The detailed procedure of graphite electrode preparation can refer to our previous paper<sup>[37]</sup>. After drying naturally, the prepared graphite electrode was transferred to a vacuum oven at 80 °C and dried overnight. Then, the graphite electrode was slightly calendered and punched into disks with a diameter of 1.5 cm. The capacity ratio between graphite and positive electrodes (referred to N/P ratio) was controlled at 1.12. 1M LiPF<sub>6</sub> in EC/EMC (3:7 in weight) with 2.0 wt% vinylene carbonate (VC) was used as electrolyte in Graphite||NMC76 full coin cells. All the cells were tested at 0.1C/0.1C for the formation cycles and then cycled at 0.33C/0.33C with the cutoff voltage of 4.2 V or 4.45 V at 25 °C.

*Pouch cell.* Single layer pouch cells were prepared and assembled in the dry room (0.1 RH%, 19 °C) of the Advanced Battery Facility Laboratory at PNNL. The corresponding cathode and anode sizes are 54 mm\*36 mm and 55.5 mm\*37.5 mm, respectively. The slurry ratios in NMC cathode and graphite anode are the same as in coin cells, and all the testing conditions were maintained the same as the full coin cells. The applied cathode electrode loading is around 12 mg cm<sup>-2</sup>. The corresponding voltage profiles were presented at **Fig. S11**.

### **Scanning electron microscope (SEM)**

The morphologies of polycrystalline and single-crystalline NMC76 were investigated by scanning electron microscope (SEM, Helios).

### **Scanning transmission electron microscopy (STEM)**

The electrode particles were harvested and washed by dimethyl carbonate (DMC), followed by preparation of STEM specimens with a focused ion beam (FIB) lifting out procedures using a Thermo Scientific Helios DualBeam working at 2-30 keV. STEM imaging was performed on the aberration corrected JEOL JEM-ARM200CF with the operating voltage of 200 kV. The convergence semi-angle is 20.6 mrad, and the signals with semi-angles spanning from 68 to 280 mrad were collected for STEM HAADF imaging.

### **Electron energy loss spectroscopy (EELS)**

EELS microanalysis data were collected on the aberration corrected JEOL JEM-ARM200CF with the operating voltage of 200 kV, and a post-column Gatan Image Filter (GIF) working at 0.25 eV/channel energy dispersion. The convergence semi-angle for the electron probe is 20.6 mrad and the EELS collection semi-angle is 42.9 mrad. The EELS spectra were processed by subtraction of the pre-edge power-law background using the Digital Micrograph software.

### ***In situ* electrochemical AFM measurements**

The preparation of AFM working electrodes and the *in situ* AFM setting are following our previous work<sup>[5]</sup>. The applied voltage started at OCV and charged to 4.9 V, with a uniform scan rate of 0.3 mV s<sup>-1</sup>.

### **Gas measurements**

*Online testing parameters.* *In situ* differential electrochemical mass spectrometry (DEMS) analysis was carried out to detect the gases generated during electrochemical testing. Here, Ar was selected as inert carrier gas and the corresponding flow rate is 30 mL/min. The equipped mass spectrometer was HPR-40 (Hiden Analytical Ltd.) with a constant flow rate of 12.5  $\mu$ L/min. The electrochemical cell coupled with MS was a commercial ECC-DEMS cell (ECC-Air), labeled as E-cell. Working electrodes used in E-cell are the pristine and cycled positive electrodes in full coin cells. Before assembly in E-cell, the disassembled cycled electrodes were washed with DMC in Ar-filled glovebox. After the washed electrodes were dried naturally in vacuum for 48h, they were pierced by a needle to make holes for gas passing during test. The corresponding electrode loading is ca. 12 mg/cm<sup>2</sup>. To exclude the effect of electrode loading on gas generation analysis, gas evolution in high loading electrodes was also collected for comparison (Fig. S12). There are not much difference in the gas generation contents between the two loadings at the first 3 cycles. The counter and reference electrodes are Li metal, and porous glass microfiber paper (GF/D, Whatman) was used as the separator. The corresponding electrolyte is 1M LiPF<sub>6</sub> in ethyl carbonate (EC) and ethyl methyl carbonate (EMC) (3:7 by weight), and the content is 400  $\mu$ L, which floods electrodes and separator, and does not block the tube for gas diffusion and makes sure the sensitivity during the *in situ* testing. During *in situ* DEMS measurement, the applied electrolyte didn't involve VC additive. Because, in practical applications, additive content is limited in the electrolyte, which might be used out during the formation cycles, and it contributes to building a stable interface between electrode and electrolyte, suppressing the reaction between the two parts and acting as a

gas reducing agent<sup>[38, 39]</sup>. Therefore, extra additive in the electrolyte affects the gas generation behaviors of the electrode materials during cycling. (Fig. S13) So, for independent gas evolution research on cathode materials, electrolyte without additives can better reflect the real situation. The charge/discharge rates are 0.2C, and the cutoff voltages in E-cells are 0.5 V higher than that in full coin cells, which are 4.25 V and 4.5 V. After 200 cycles, when the cycled polycrystalline NMC76 electrode was tested at 0.2C in E-cell, no big difference between its capacities compared to the coin cell performance (Fig. S14). However, the capacities of single crystal NMC76 were lower than that in coin cells around 200 cycles at 0.33C (Fig. S14), which can be attributed to the increasing interface impedance<sup>[40]</sup>. Hence, the single crystal NMC76 electrode after 200 cycles tested in E-cell at 0.2C cannot reflect the real gas evolution. (Fig. S15) Accordingly, single crystal and polycrystalline NMC76 electrodes after 200 cycles were tested in E-cell at 0.1C to maintain the capacities achieved in coin cells.

*Pouch cell gas testing.* The detailed testing procedure of the accumulated gases generated in a single-layer pouch cell was presented in Fig. 3b. The cycled pouch cells were first placed under 1000 kgf press machine and held for 5 mins to exhaust the residual gas between electrodes and separator. Then, a gas-tight syringe (10  $\mu$ L) was applied to transfer the resultant gas from the pouch bag into the home-made three-windows tube connected with carrier gas and MS. During gas extraction with a syringe, a small amount of air was left in the needle space and was tested together with evolved gas. Moreover, owing to the limited gas content in a single-layer pouch cell, some electrolyte was collected with the generated gases and injected into the three-windows tube, resulting in fragments generated in the MS affecting the background. A controlled experiment was carried out to exclude these effects. We collected the used organic electrolyte with the same syringe in the atmosphere and injected it into the three-windows tube for gas testing, which was designed to build a background curve for the pouch cell gas measurement.

*Gas percentage calculation.* H<sub>2</sub>, CO, C<sub>2</sub>H<sub>4</sub>, CO<sub>2</sub>, O<sub>2</sub>, and Ar were monitored, tested, and labeled as n. The total pressure ( $P_{total}$ ) is a summation of each corrected portion ( $P_n$ ), and the relevant calculation processes are as follows:

$$P_{total} = \sum_1^n P_n \text{ (} P_n \text{ is gas partial pressure of gas n).}$$

$$P_n = [(G_n - SS_n)/(RS_n)]$$

( $G_n$  is the raw value,  $SS_n$  is the spectral subtraction from contributions of other gasses to gas n, and  $RS_n$  is the relative sensitivity for gas n.)

$$SS_n = G_{n'} * \text{fragmentation proportion that contributes to n.}$$

( $G_{n'}$  is another gas in the matrix.)

$$PPM(n) = 10^6 \frac{P_n}{P_{total}}$$

*Gas evolution rate calculation.* Accordingly, with the gas percentage and flow rate (12.5  $\mu\text{L}/\text{min}$ ) in the mass spectrometer, the gas evolution rate can be calculated. In this paper, the m/z values of H<sub>2</sub>, O<sub>2</sub>, C<sub>2</sub>H<sub>4</sub>, CO<sub>2</sub>, and Ar are set as 2, 14, 32, 27, 44, and 40<sup>[24, 41]</sup>. However, CO does not have a unique m/z channel because its m/z=28 channel is disturbed by C<sub>2</sub>H<sub>4</sub> and CO<sub>2</sub>. Hence, to calculate the fraction of CO in m/z = 28, x times the signal of m/z = 27 and y times the signal of m/z = 44 should be subtracted. x and y are the fractions of C<sub>2</sub>H<sub>4</sub> and CO<sub>2</sub> on m/z = 28 compared to their unique signals on m/z=27 (C<sub>2</sub>H<sub>4</sub>) and m/z=44 (CO<sub>2</sub>), which are 1/0.648 and 0.114, respectively.

*Gas calibration.* Here, two kinds of standard gases were used to calibrate H<sub>2</sub>, O<sub>2</sub>, CO<sub>2</sub>, C<sub>2</sub>H<sub>4</sub>, and CO, which are Ar with 2000 ppm each of H<sub>2</sub>, O<sub>2</sub>, C<sub>2</sub>H<sub>4</sub>, and CO<sub>2</sub> and Ar with 2000 ppm each of H<sub>2</sub>, O<sub>2</sub>, CO, and CO<sub>2</sub> (Nor LAB), respectively. For calibration, the following equation is used:

$$\frac{G_{Ar}}{RS_{Ar} * \%_{Ar}} = \frac{G_n}{RS_n * \%_n}$$

( $RS_n$  is relative sensitivity of gas n,  $\%_n$  is the percentage in the known mixture). Here, we set the  $RS_{Ar}$  value as 1. Normally, calibration gas with only one component and concentration will induce a certain error during the measurements by contamination and background. Here, two calibration gases were applied, realizing mutual verification of the calibration data. Moreover, during calibration, 3 points were selected to obtain an average value for sufficient calibration. (Fig. S16a,b) The multi-point calibration using two calibration gases makes the final results more accurate and reliable. On channel m/z=28, except CO and C<sub>2</sub>H<sub>4</sub>, N<sub>2</sub> also has a contribution. Here, in our equipment, Ar with 2000 ppm each of H<sub>2</sub>, O<sub>2</sub>, C<sub>2</sub>H<sub>4</sub>, and CO<sub>2</sub> was applied to calculate the contribution of N<sub>2</sub>. After 0.4h test, the real content of N<sub>2</sub> on m/z=28 is closed to zero, proving the high tightness of the test equipment and purity of calibration gases. (Fig. S16c) The final calibrated

RS values were summarized, including H<sub>2</sub> (0.86), O<sub>2</sub> (0.84), CO<sub>2</sub> (0.74), C<sub>2</sub>H<sub>4</sub> (0.932) and CO (0.949). (Fig. S16d) All the gas evolution data was tested at least twice as shown in Table S3 to make sure the presented data are solid and repeatable.

## Author Contributions

J.H. and J.X. conceived the ideas and designed the experiments. L.L. and C.W. performed the TEM experiments and analyses. Y.B. offered the single crystal NMC. J.T. and J.H. conducted the *in situ* AFM test. J.L. helped with manuscript polish and data discussion. D.L. and J.H. prepared the pouch cell. B.W. and X.C. analyzed the data. S.C. helped draw the schematic diagram. The manuscript was written by J.H. and J.X. All authors reviewed and approved the manuscript.

## Conflicts of interest

There are no conflicts to declare.

## Acknowledgements

This work was supported by the Assistant Secretary for Energy Efficiency and Renewable Energy, Office of Vehicle Technologies of the U.S. Department of Energy (DOE) through the Applied Battery Research Program under contract no. DE-LC-000L053. PNNL is a multiprogram national laboratory operated by Battelle for the DOE under contract DE-AC05-76RL01830.

## References

- [1] H. H. Sun, H.-H. Ryu, U.-H. Kim, J. A. Weeks, A. Heller, Y.-K. Sun and C. B. Mullins, *ACS Energy Lett.*, 5 (2020) 1136-1146.
- [2] H.-J. Noh, S. Youn, C. S. Yoon and Y.-K. Sun, *J. Power Sources*, 233 (2013) 121-130.
- [3] Z. Chen, J. Wang, D. Chao, T. Baikie, L. Bai, S. Chen, Y. Zhao, T. C. Sum, J. Lin and Z. Shen, *Sci. Rep.*, 6 (2016) 25771.
- [4] J. Zheng, P. Yan, L. Estevez, C. Wang and J.-G. Zhang, *Nano Energy*, 49 (2018) 538-548.
- [5] J. Hu, L. Li, E. Hu, S. Chae, H. Jia, T. Liu, B. Wu, Y. Bi, K. Amine, C. Wang, J. Zhang, J. Tao and J. Xiao, *Nano Energy*, 79 (2021) 105420.
- [6] H.-H. Ryu, K.-J. Park, C. S. Yoon and Y.-K. Sun, *Chem. Mater.*, 30 (2018) 1155-1163.
- [7] M. Yoon, Y. Dong, J. Hwang, J. Sung, H. Cha, K. Ahn, Y. Huang, S. J. Kang, J. Li and J. Cho, *Nat. Energy*, 6 (2021) 362–371.
- [8] G.-L. Xu, Q. Liu, K. K. S. Lau, Y. Liu, X. Liu, H. Gao, X. Zhou, M. Zhuang, Y. Ren, J. Li, M. Shao, M. Ouyang, F. Pan, Z. Chen, K. Amine and G. Chen, *Nat. Energy*, 4 (2019) 484-494.

- [9] P. Yan, J. Zheng, J. Liu, B. Wang, X. Cheng, Y. Zhang, X. Sun, C. Wang and J.-G. Zhang, *Nat. Energy*, 3 (2018) 600-605.
- [10] H.-H. Sun and A. Manthiram, *Chem. Mater.*, 29 (2017) 8486-8493.
- [11] H. Cha, J. Kim, H. Lee, N. Kim, J. Hwang, J. Sung, M. Yoon, K. Kim and J. Cho, *Adv. Mater.*, 32 (2020) 2003040.
- [12] Y. Liu, J. Harlow and J. Dahn, *J. Electrochem. Soc.*, 167 (2020) 020512.
- [13] Y. Bi, J. Tao, Y. Wu, L. Li, Y. Xu, E. Hu, B. Wu, J. Hu, C. Wang, J.-G. Zhang, Y. Qi and J. Xiao, *Science*, 370 (2020) 1313–1317.
- [14] Y. R. Dougassa, C. Tessier, L. El Ouatani, M. Anouti and J. Jacquemin, *J. Chem. Thermodynamics*, 61 (2013) 32-44.
- [15] Z. Khodr, C. Mallet, J.-C. Daigle, Z. Feng, K. Amouzegar, J. Claverie and K. Zaghbi, *J. Electrochem. Soc.*, 167 (2020).
- [16] J. Wandt, A. T. S. Freiberg, A. Ogrodnik and H. A. Gasteiger, *Mater. Today*, 21 (2018) 825-833.
- [17] T. Hatsukade, A. Schiele, P. Hartmann, T. Brezesinski and J. Janek, *ACS Appl. Mater. Interfaces*, 10 (2018) 38892-38899.
- [18] S. E. Renfrew and B. D. McCloskey, *J. Am. Chem. Soc.*, 139 (2017) 17853-17860.
- [19] R. Jung, M. Metzger, F. Maglia, C. Stinner and H. A. Gasteiger, *J. Electrochem. Soc.*, 164 (2017) A1361-A1377.
- [20] R. Jung, P. Strobl, F. Maglia, C. Stinner and H. A. Gasteiger, *J. Electrochem. Soc.*, 165 (2018) A2869-A2879.
- [21] N. Li, S. Sallis, J. K. Papp, J. Wei, B. D. McCloskey, W. Yang and W. Tong, *ACS Energy Lett.*, 4 (2019) 2836-2842.
- [22] M. Metzger, B. Strehle, S. Solchenbach and H. A. Gasteiger, *J. Electrochem. Soc.*, 163 (2016) A798-A809.
- [23] R. Jung, M. Metzger, F. Maglia, C. Stinner and H. A. Gasteiger, *J. Phys. Chem. Lett.*, 8 (2017) 4820-4825.
- [24] B. B. Berkes, A. Jozwiuk, M. Vracar, H. Sommer, T. Brezesinski and J. Janek, *Anal. Chem.*, 87 (2015) 5878-5883.
- [25] J. Xiao, J. Hu, D. Wang, D. Hu, W. Xu, G. L. Graff, Z. Nie, J. Liu and J.-G. Zhang, *J. Power Sources*, 196 (2011) 5674-5678.
- [26] B. D. McCloskey, A. Speidel, R. Scheffler, D. C. Miller, V. Viswanathan, J. S. Hummelshoj, J. K. Nørskov and A. C. Luntz, *J. Phys. Chem. Lett.*, 3 (2012) 997-1001.
- [27] Z. Zhang, J. Lu, R. S. Assary, P. Du, H.-H. Wang, Y.-K. Sun, Y. Qin, K. C. Lau, J. Greeley, P. C. Redfern, H. Iddir, L. A. Curtiss and K. Amine, *J. Phys. Chem. C*, 115 (2011) 25535-25542.
- [28] X. Wang and C. K. Law, *J. Chem. Phys.*, 138 (2013) 134305.
- [29] C. Xu, K. Marker, J. Lee, A. Mahadevegowda, P. J. Reeves, S. J. Day, M. F. Groh, S. P. Emge, C. Ducati, B. Layla Mehdi, C. C. Tang and C. P. Grey, *Nat. Mater.*, 20 (2021) 84-92.
- [30] J. Zheng, P. Yan, J. Zhang, M. H. Engelhard, Z. Zhu, B. J. Polzin, S. Trask, J. Xiao, C. Wang and J. Zhang, *Nano Res.*, 10 (2017) 4221-4231.
- [31] L. Wu, K.-W. Nam, X. Wang, Y. Zhou, J.-C. Zheng, X.-Q. Yang and Y. Zhu, *Chem. Mater.*, 23 (2011) 3953-3960.
- [32] K.-W. Nam, S.-M. Bak, E. Hu, X. Yu, Y. Zhou, X. Wang, L. Wu, Y. Zhu, K.-Y. Chung and X.-Q. Yang, *Adv. Funct. Mater.*, 23 (2013) 1047-1063.

- [33] A. Tornheim, S. Sharifi-Asl, J. C. Garcia, J. Bareño, H. Iddir, R. Shahbazian-Yassar and Z. Zhang, *Nano Energy*, 55 (2019) 216-225.
- [34] L. Li, J. Hu, J. Xiao and C. Wang, *Acs Applied Materials & Interfaces*, 13 (2021) 18849-18855.
- [35] Y. B. He, B. Li, M. Liu, C. Zhang, W. Lv, C. Yang, J. Li, H. Du, B. Zhang, Q. H. Yang, J. K. Kim and F. Kang, *Sci. Rep.*, 2 (2012) 913.
- [36] X. Li, K. Qian, Y.-B. He, C. Liu, D. An, Y. Li, D. Zhou, Z. Lin, B. Li, Q.-H. Yang and F. Kang, *Journal of Materials Chemistry A*, 5 (2017) 18888-18895.
- [37] J. Hu, B. Wu, S. Chae, J. Lochala, Y. Bi and J. Xiao, *Joule*, 5 (2021) 1011-1015.
- [38] J. Xia, C. P. Aiken, L. Ma, G. Y. Kim, J. C. Burns, L. P. Chen and J. R. Dahn, *J. Electrochem. Soc.*, 161 (2014) A1149-A1157.
- [39] M. Holzapfel, A. Würsig, W. Scheifele, J. Vetter and P. Novák, *J. Power Sources*, 174 (2007) 1156-1160.
- [40] X. Chen, Y. Tang, C. Fan and S. Han, *Electrochim. Acta*, 341 (2020) 136075.
- [41] R. Imhof and P. Novak, *J. Electrochem. Soc.*, 145 (1998) 1081-1087.

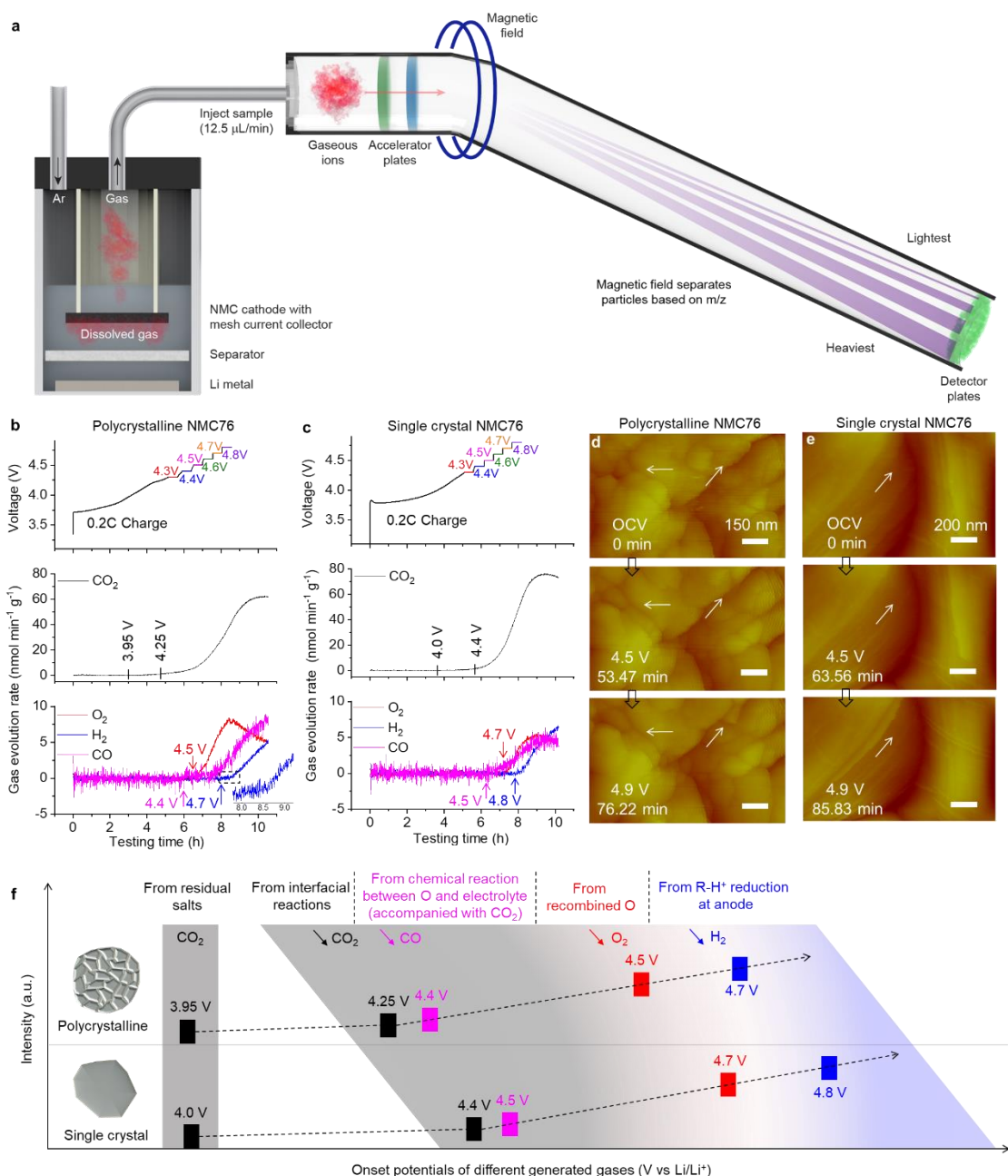


**Fig. 1** Scheme for *in situ* DEMS construction, gas generation analysis and surface morphology evolution of polycrystalline and single crystal NMC76. a) Schematic diagram presenting the construction of the *in situ* DEMS system. b,c) Gas evolution during the potential stepping procedures as a function of electrode potential for polycrystalline NMC76 (b) and single crystal NMC76 (c). The cells are firstly charged to 4.3 V. From 4.3 V to 4.8 V, the potentials applied on the cell are gradually elevated with a step size of 0.1 V and held for 0.5 hour at each potential. *Upper panels in (b) and (c)*: cell voltage vs. time of polycrystalline and single crystal NMC76 with Li-metal as the counter electrode in E-cell charged to 4.8 V at 0.2 C (1C = 200 mA/g); *center panels in (b) and (c)*: CO<sub>2</sub> evolution rate measured by *in situ* DEMS; *lower panels in (b) and (c)*: gas evolution rates for O<sub>2</sub>, H<sub>2</sub> and CO. d,e) Microstructural evolution of polycrystalline NMC76 (d) and single crystal NMC76 (e) captured by *in situ* AFM in a functioning electrochemical cell charged to 4.9 V. f) Summary and comparison of gas generation in polycrystalline and single crystal NMC76 during charge.

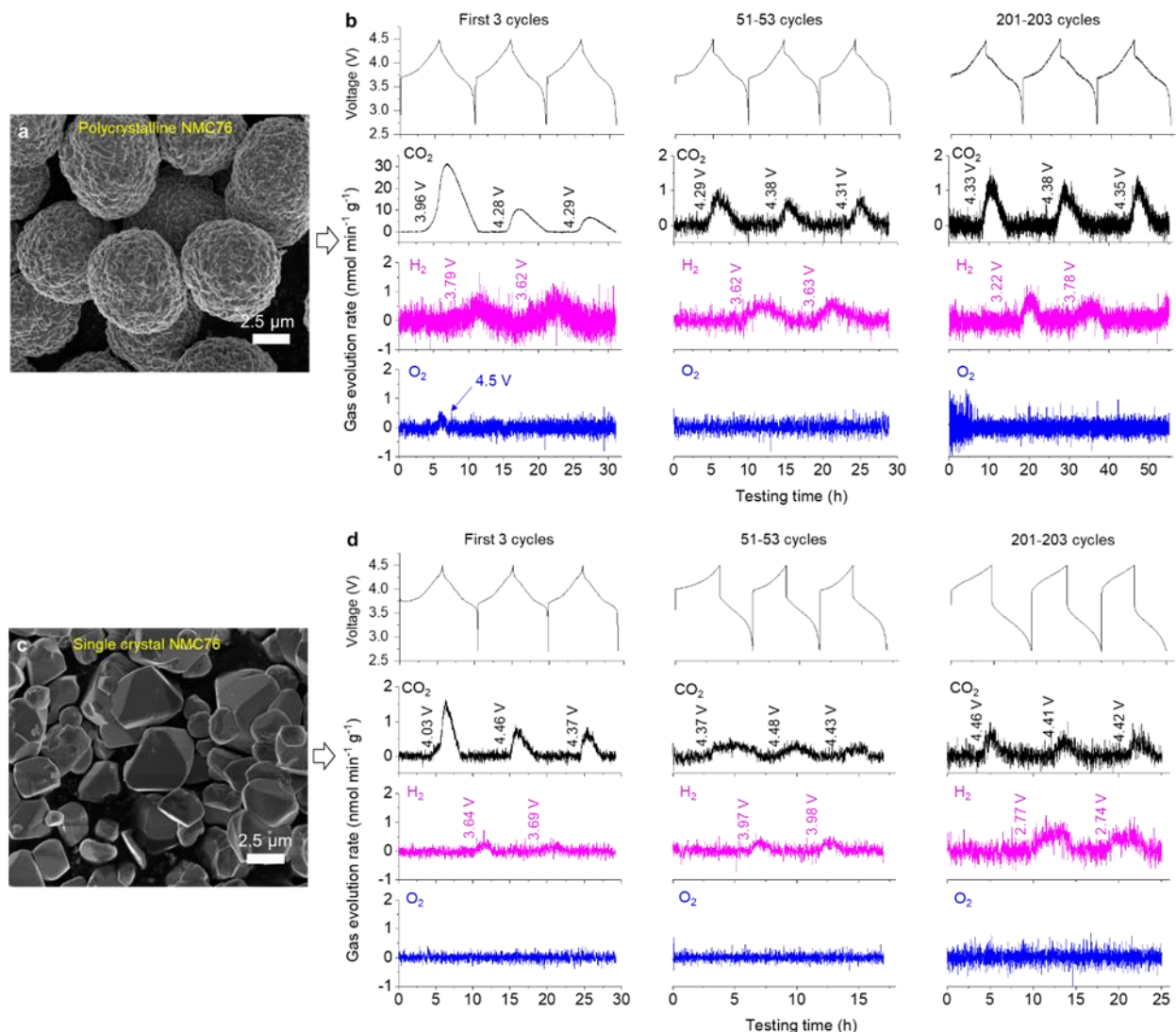


**Fig. 2** Comparison of gas evolution in E-Cells with polycrystalline and single crystal NMC76 as electrodes. a,c) Morphologies of pristine polycrystalline NMC76 (a) and single crystal NMC76 (c). b,d) Evolution of CO<sub>2</sub>, H<sub>2</sub>, and O<sub>2</sub> at different cycles of polycrystalline NMC76 (b) and single crystal NMC76 (d) electrodes. The corresponding voltage interval in E-cell is between 2.7 V and 4.5 V (vs. Li/Li<sup>+</sup>). The electrodes used for the 51-53 and 201-203 cycles' tests were first completed 50 and 200 cycles in full coin cells with a cutoff voltage of 4.45 V (vs. graphite). *Upper panels in (b) and (d)*: voltage profiles of polycrystalline and single crystal NMC76 electrodes at different cycles; *2<sup>nd</sup> panels in (b) and (d)*: CO<sub>2</sub> evolution rates at different cycles; *3<sup>rd</sup> panels in (b) and (d)*: H<sub>2</sub> evolution rates at different cycles; *lower panels in (b) and (d)*: O<sub>2</sub> evolution rates at different cycles.

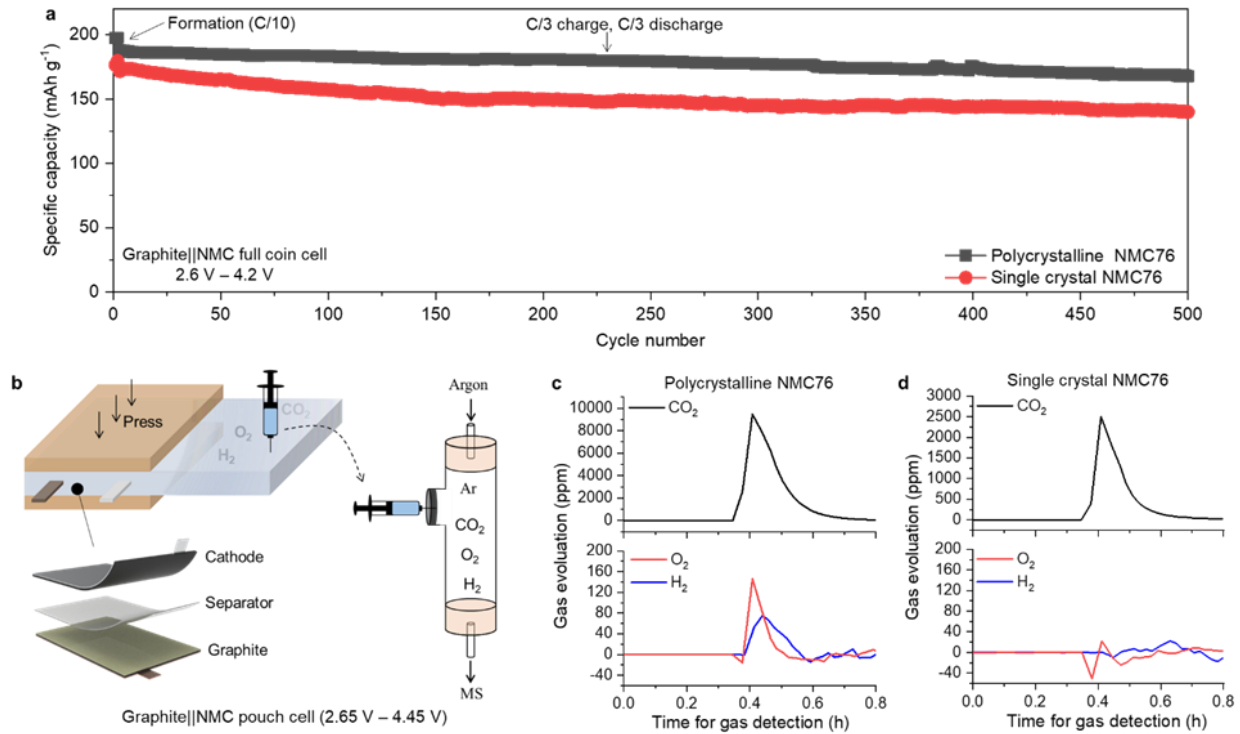


**Fig. 3** Gas analysis of polycrystalline and single crystal NMC76 in pouch cells. a) Cycling stability of polycrystalline and single crystal NMC76 with graphite as the counter electrode. The cells are cycled between 2.7 V and 4.2 V using graphite as the anode in coin cells. The mass loading of NMC76 is around  $12 \text{ mg cm}^{-2}$ . b) Schemes for single layer pouch cell for gas collection and transfer. c,d) Quantified amounts of CO<sub>2</sub>, O<sub>2</sub>, and H<sub>2</sub> in pouch cells after 200 cycles of polycrystalline NMC76 (c) and single crystal NMC76 (d).

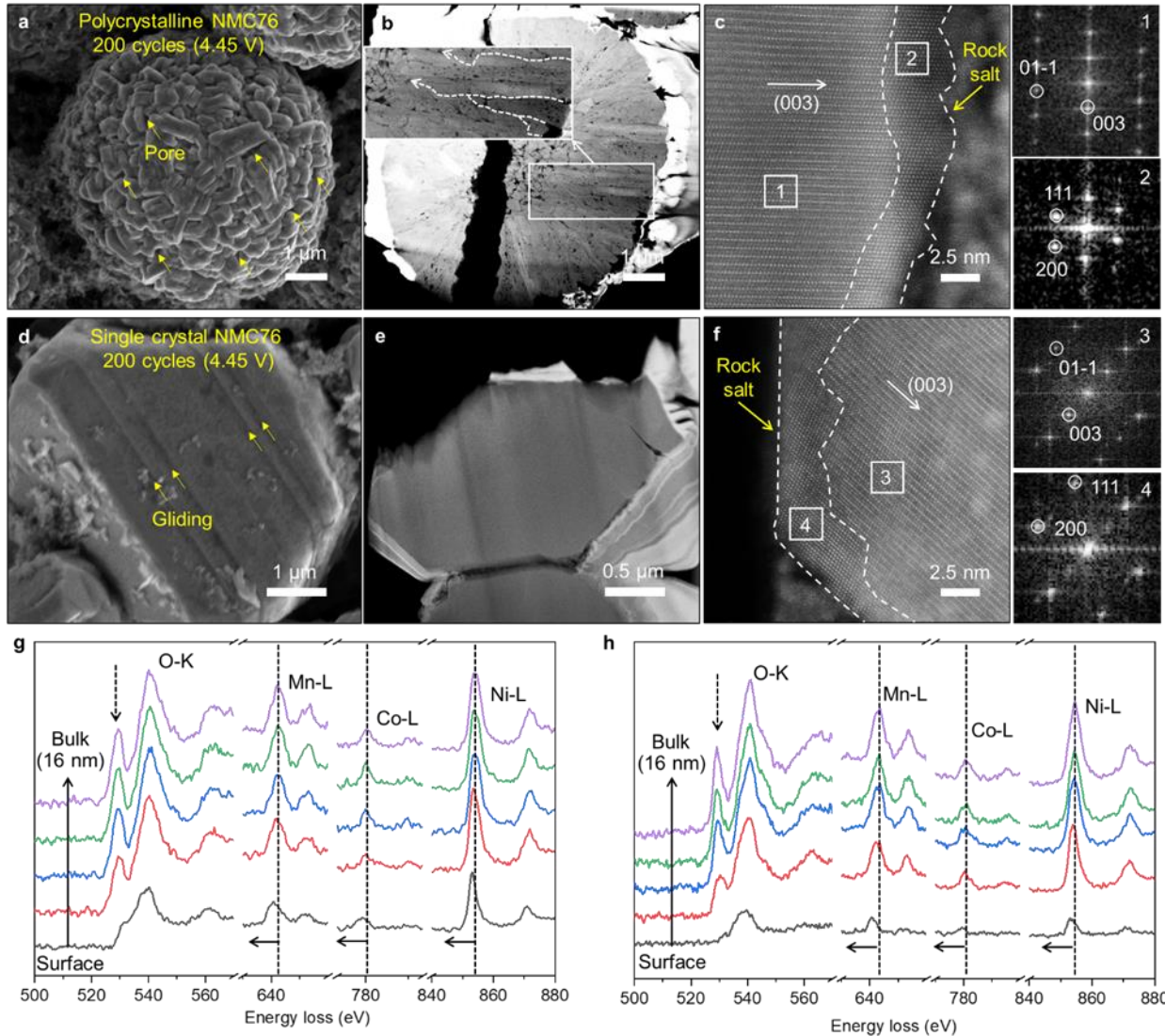


**Fig. 4** Structural characterizations of cycled polycrystalline and single crystal NMC76. a-c) Polycrystalline NMC76 after 200 cycles in full cells with a cutoff voltage at 4.45 V (vs. graphite). (a) SEM image of the cycled polycrystalline NMC76. (b) Cross-sectional HAADF-STEM image of the cycled polycrystalline NMC76. (c) HAADF-STEM image presenting phase change on the particle surface of the cycled polycrystalline NMC76. The corresponding fast Fourier transform of region 1 and region 2 show layered structure and rock-salt structure, respectively. d-f) Single crystal NMC76 after 200 cycles in full cells with a cutoff voltage of 4.45 V (vs. graphite). (d) SEM image of the cycled single crystal NMC76. (e) Cross-sectional HAADF-STEM image of the cycled single crystal NMC76. (f) HAADF-STEM image and fast Fourier transform of the cycled single crystal NMC76. The corresponding fast Fourier transform of region 3 and region 4 show layered structure and rock-salt structure, respectively. g,h) EELS spectra of the O *K*-edges and Mn, Co, and Ni *L*-edges collected at 5 different locations from surface to bulk; the corresponding testing depth is around 16 nm, including polycrystalline NMC76 (g) and single crystal NMC76 (h) after 200 cycles with a cutoff voltage of 4.45 V (vs. graphite).